**Proceedings of the ASME 2018 International Mechanical Engineering Congress and Exposition**
**IMECE2018**
**November 9-15, 2018, Pittsburgh, PA, USA**

# IMECE2018-86615

# COMPUTATIONAL DESIGN OF A BIRD-INSPIRED PERCHING LANDING GEAR MECHANISM

**Paul M. Nadan**
Franklin W. Olin College of Engineering
Needham, MA, USA

**Christopher L. Lee**
Franklin W. Olin College of Engineering
Needham, MA, USA

## ABSTRACT

To support the design of a mechanism with two opposing, underactuated, multi-segmented feet that enables a small UAV to grasp and perch upon a branch or similar structure, a hybrid empirical-computational model has been developed that can be used to predict whether the mechanism can kinematically grasp structures with a range of cross-section shapes and sizes in various orientations and to quantify the forces exerted by the grasp. The model, based on experimentally-determined parameters, relates the curvature of the feet to the displacement and tension of the cable tendon which is related in turn to the weight of the UAV. The working principle of the landing gear follows the anatomy of birds that grasp and perch as tendons in their legs and feet are tensioned. Results demonstrate how the model can be used to simulate and evaluate grasping in order to determine the size and weight of a UAV for landing and perching upon a range of target structures.

## INTRODUCTION

Small multirotor, fixed-wing, and flapping-wing unmanned aerial vehicles (UAV) are being used in a rapidly-broadening range of civil and mililtary applications. Missions often call for operation in urban or rural settings that do not have appropriate or sufficiently large space for take-off and landing. In such areas, the capability for a UAV to land upon, perch, and takeoff from available structures and surfaces would enable it to perform its missions.

To smoothly alight on a structure like a bird, a UAV would have to execute a series of intricate flight manuevers involving complex path planning and trajectory control [1]. To this end, Robertson and Reich [2] conducted controlled flight tests to land and perch small fixed-wing planes with bird-like planforms on a target platform. Nagendran *et al.* [3] evaluated controllers to softly land a UAV with a two-jointed leg on a surface. Paranjape *et al.* [4] designed and experimentally demonstrated a guidance and control scheme to land and perch a fixed-wing micro aerial vehicle equipped with articulated wings. In Ref. [5], Cory and Tendrake designed and tested optimal control policies for the elevator deflection so a small fixed-wing automonous glider could execute high angle-of-attack maneuvers needed to land on a suspended horizontal string.

In addition to controlling their flight to perch, birds use their feet to grasp ahold of the structures or objects that they are landing on. UAV's can do likewise by employing a clamping or grasping mechanism. Culler *et al.* [6] designed and tested a compliant, bi-stable snapping-claw mechanism that is triggered by the impact of landing. In Ref. [7], Ali Erbil *et al.* used a design optimization procedure to identify a configuration for a four-legged, motor-driven gripper that can clamp onto a cylindrical projection bracket. Using a two-dimensional model to inform their design process, Chi *et al.* [8] developed and tested a mechanically-similar, four-legged, servo-driven gripper. Jiang *et al.* [9] created a model of an opposing-grip mechanism with adhesive contact surfaces embedded with micro-spines for perching on walls and ceilings. They conducted experiments to validate mechanical aspects of their model. Burroughs and her co-authors [10] modeled and fabricated a Sarrus-linkage-based clamping mechanism for a rotorcraft to perch on cylindrical 'branches.' The mechanism is actuated by the weight of the air vehicle.

This passive acutation is the working principle for the legs of many types of birds [11]. When landing and coming to a rest, the joints in their legs rotate and the bird's weight tensions tendons causing the foot to wrap around the object it encloses. When the bird takes off, the tendons relax from their stretched position and the grip is released. Backus *et al.* [12] modeled the grasping behavior of a simplied bird foot model to analyze the force imparted when carrying and perching and to study their relation to anatomy geometry. In Ref. [13], they performed mechanical analysis on a tendon-actuated hand to determine the effects of geometric parameters on grasping and perching. Doyle *et al.* [14-15] presented work on a perching mechanism based upon a collapsing leg with tendon-actuated gripping feet. Static tests demonstrated that a quadcopter could successfully perch on a variety of commonly available objects. Xie *et al.* [16-17] presented modeling, simulation, and analyses for the design of a

 

cable-tensioned, three-digit foot. A prototype could grasp a wide variety of objects; however, the force applied was significantly reduced by friction in the joints. In addition, the entire leg-foot system was too large and heavy to incorporate in a small UAV.

In Ref [18], Tieu *et al.* demonstrated the feasibility of a bird-inspired, landing gear system that could grasp ahold of branch-like objects and enable a UAV to perch. To support the design and optimization of these specific mechanisms, a hybrid empirical-numerical model has been developed that can kinematically predict whether the mechanism is able to grasp structures with a range of cross-section shapes, dimensions, and orientations and to quantify forces exerted while grasping. The model is described herein along with validation experiments comparing simulations to the performance of a prototype landing gear system attached to a hexacopter.

## PERCHING LANDING GEAR MECHANISM

The landing gear system consists of two legs attached to the bottom of the air vehicle; see Fig. 1. Each leg is a four-bar linkage. Both legs are connected to an axel through bearings incorporated into the top joint or 'hip' of each linkage. The rotation of the axel can be actuated with a motor or locked in place. At the bottom of each leg are opposing flexible feet which are offset to one another on a flat palm.

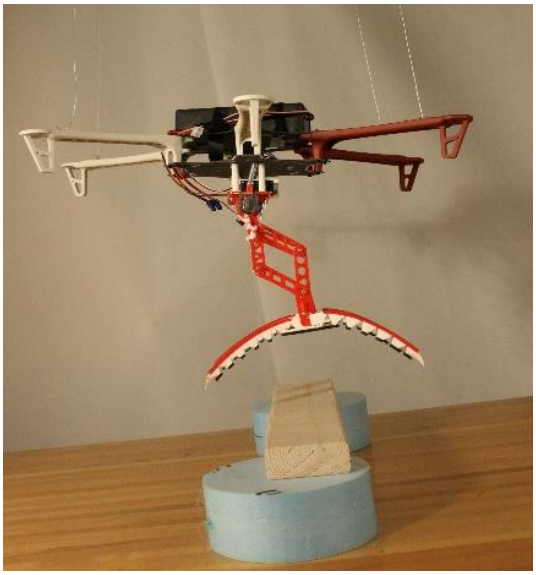

**Fig. 1 The bird-inspired, perching landing gear, attached to a suspended hexacopter body, consists of four-bar-linkage legs with cable-tendon-acutated, multi-segmented, flexible feet**

Each foot (an example is shown in Fig. 2) is a single, compliant structure fabricated by simultaneouly 3D-printing a flexible thermo-plastic (NinjaFlex, Ninjatek, Manheim, PA) and a stiff plastic (ABS filament, Makerbot, Brooklyn, NY). Six stiff segments (white) are connected at their bases by two flexible rails (red). Two features were included to prevent the claw end from curling closed before the target could be grasped. The first is the height of each segment is graduated from highest near the base to lowest at the claw end creating larger bending moments on the rails towards the base. The second is the rails themselves taper slightly going from the claw end back to the base. The area moment of inertia of the cross-section decreases which decreases the bending stiffness towards the base. Soft pads (black in Fig. 1) were attached to the faces of each segment to improve grip.

The feet are actuated by cable tendons with one end fixed to the claw segment of the foot and the other end fixed to the hip of the leg. The tendon is thread freely through each segment of the foot and wraps around pulleys inside the linkage.

**Fig. 2 A six-segment, compliant foot fabricated by 3D printing a flexible thermal-plastic (red) and stiff ABS (white). Length: 13 cm. Segment heights: 0.9-1.7cm.**

As the UAV lands, its weight collapses the four-bar linkage pulling the tendons causing the feet to curl and grasp the landing target. Figure 3 shows a bare-frame and fully-loaded hexacopter stably perched on a wood board and a tree branch.

**Fig. 3 A hexacopter frame and a flight-ready hexacopter stably perch on a wood board and on a tree branch. The weight of the air vehicle tensions cable tendons which curl the feet and grasp.**

## HYBRID EMPIRICAL-NUMERICAL MODEL FOR GRASP ANALYSIS

A hybrid empirical-numerical model has been created for simulating the mechanical behavior of the landing gear. The entire mechanism is abstracted to be planar. A flowchart for the model is shown in Fig. 4. Empirical relationships (cubic polynomials) relate the four-bar geometry and the relative rotation angles of the segments of the feet. The positions of the segments are then tested for contact with the target object. If there is contact, the forces applied by the feet on the object are computed using another empirical relationship (cubic polynomial) relating the tendon tension with the tendon displacement. Finally, a determination is made as to whether the mechanism has successfully grasped the target.

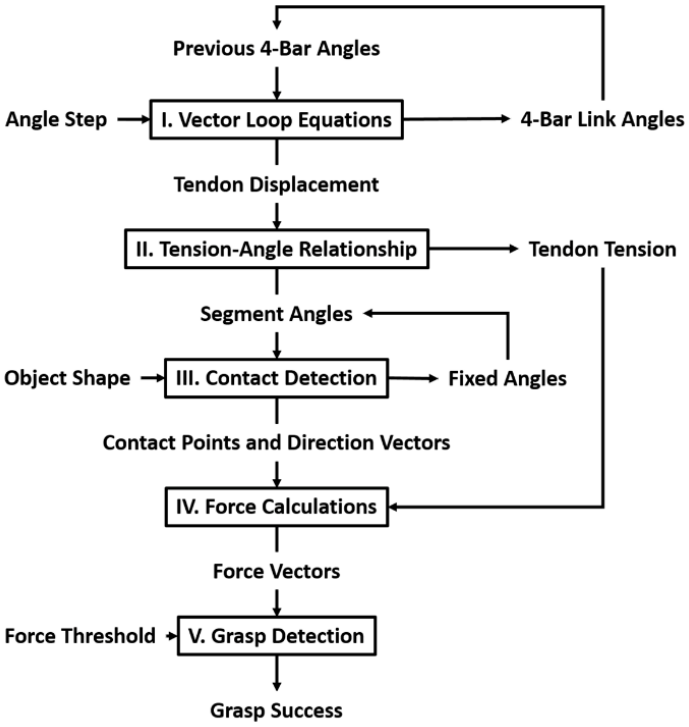


**Fig. 4 Flowchart for the hybrid empirical-numerical model**

*I. Four-Bar Linkage Simulation*

As the four-bar linkage collapses under the weight of the UAV, the distance between the joints $J_1$ and $J_3$ (shown in Fig. 5) increases, causing a reduction in the length of tendon within the foot. The collapse kinematics are simulated in MATLAB (MathWorks, Natick MA) using the following vector loop equations

$$L_1 \sin(\theta_1) + L_2 \sin(\theta_2) + L_3 \sin(\theta_3) + L_4 \sin(\theta_4) = 0$$
$$L_1 \cos(\theta_1) + L_2 \cos(\theta_2) + L_3 \cos(\theta_3) + L_4 \cos(\theta_4) = 0$$

$$L_2\, sin(\theta_2)\omega_2 + L_3 \cos(\theta_3)\, \omega_3 + L_4 \cos(\theta_4)\, \omega_4 = 0$$
$$-L_2\, sin(\theta_2)\omega_2 - L_3 \sin(\theta_3)\, \omega_3 - L_4 \sin(\theta_4)\, \omega_4 = 0$$

$$\begin{bmatrix} L_2\, sin(\theta_2)\omega_2 \\ L_2\, cos(\theta_2)\omega_2 \end{bmatrix} + \begin{bmatrix} L_3 \sin(\theta_3) & L_4 \sin(\theta_4) \\ L_3 \cos(\theta_3) & L_4 \cos(\theta_4) \end{bmatrix} \begin{bmatrix} \omega_3 \\ \omega_4 \end{bmatrix} = \begin{bmatrix} 0 \\ 0 \end{bmatrix}$$

$$\begin{bmatrix} \omega_3 \\ \omega_4 \end{bmatrix} = \begin{bmatrix} L_3 \sin(\theta_3) & L_4 \sin(\theta_4) \\ L_3 \cos(\theta_3) & L_4 \cos(\theta_4) \end{bmatrix}^{-1} \begin{bmatrix} -L_2\, sin(\theta_2)\omega_2 \\ -L_2\, cos(\theta_2)\omega_2 \end{bmatrix} \quad (1)$$

where $\theta_i$ is the angle of each link relative to horizontal, $\omega_i$ is the angular velocity of each link, and $L_i$ is the length of each link as shown in Fig. 5.

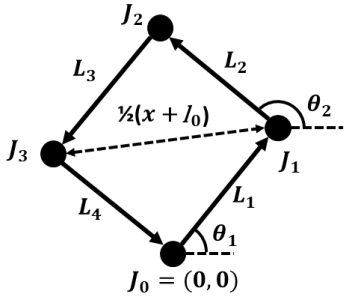


**Fig. 5 Diagram of the four-bar linkage**

The sum of the position vectors of each link equals zero because they form a closed loop. By taking the derivative with respect to time and holding $\theta_1$ constant, $\omega_3$ and $\omega_4$ can be found in terms of $\omega_2$ and the current linkage angles. Assuming a constant value for $\omega_2$, the linkage geometry can be calculated numerically [19] over the duration of the collapse starting from a known initial configuration. The position of each joint can be computed for any state of the linkage using the resulting position vectors as

$$\boldsymbol{J}_n = \sum_{i=1}^{n} L_i \cos(\theta_i)\hat{\imath} + L_i \sin(\theta_i)\,\hat{\jmath} \quad (2)$$

The tendon displacement $x$ is defined as the change in distance between joints $J_1$ and $J_3$ and can be calculated as

$$x = 2|\boldsymbol{J}_1 - \boldsymbol{J}_3| - l_0 \quad (3)$$

where $l_0$ is the distance between joints $J_1$ and $J_3$ in the linkage's initial configuration. The tendon, taken to be inextensible, loops around joints $J_1$ and $J_3$ so the total length of tendon between $J_1$ and $J_3$ is twice the distance between the joints.

*II. Tendon Tension and Segment Angle Relationship*

The tension in the cable tendon and the relative angles, $\phi_i$, between each segment of the foot (shown in Fig. 6) are related through the displacement of the tendon. The tension in the tendon was measured with a force gage as it was displaced by a known amount; see Fig 7. Similarly, the (relative) segment angles were determined by displacing the cable tendon and photographing the resulting configuration. Angle values were extracted from the images using Logger Pro (Vernier Software Technology, Beaverton, OR); see Fig 8.

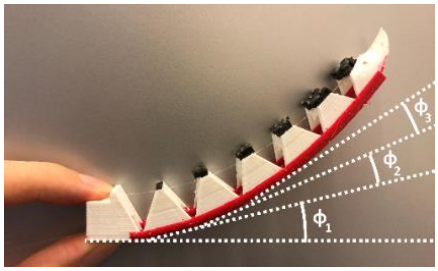


**Fig. 6 Segment angles, ϕ, are defined as the relative angles between consecutive segments of the foot**


**Fig. 7 Experimental setup for tension measurements. Gage value is halved to account for the two tendon loop on hook.**

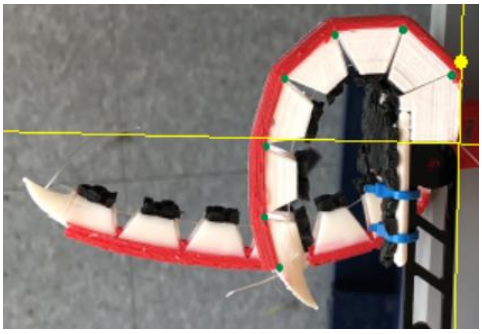

**Fig 8 Segment angles are determined using image analysis software. Segment vertices (green dots) are annotated by hand.**

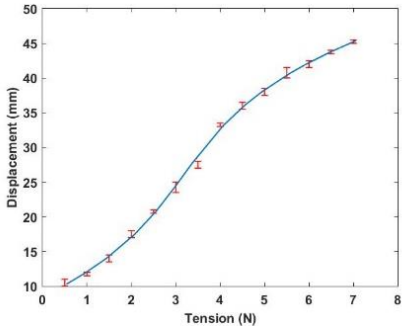


**Fig. 9 Cubic polynomial curve fit (blue line) for the measured tendon displacement vs. tendon tension (red markers). Error bars correspond to the range of measured values.**

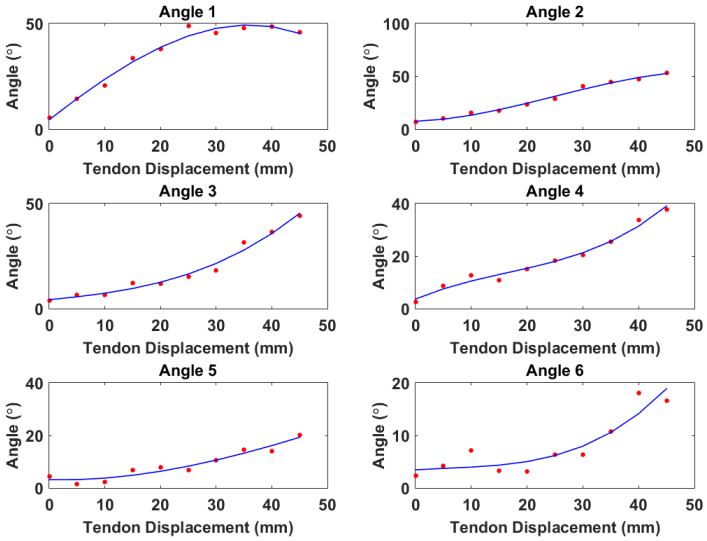


**Fig. 10 Cubic polynomial fits for observed segment angles as a function of tendon displacement**

The best fit cubic polynomials, shown in Figs. 9-10, for tendon tension, T (N), and relative segment angles, $\phi_i$ (degrees), as a function of tendon displacement, *x* (mm), were found to be

$$\begin{aligned}
\mathrm{T(x)} &= 2.2790 \times 10^{-4}\mathrm{x}^3 - 1.7690 \times 10^{-2}\mathrm{x}^2 + 5.7040 \times 10^{-1}\mathrm{x} - 3.7080 \\
\phi_1(x) &= -3.3509 \times 10^{-4}x^3 - 1.0472 \times 10^{-2}x^2 + 2.0563x + 4.5241 \\
\phi_2(x) &= -6.1532 \times 10^{-4}x^3 + 4.6033 \times 10^{-2}x^2 + 1.7948 \times 10^{-1}x + 7.5518 \\
\phi_3(x) &= 2.6197 \times 10^{-4}x^3 + 2.8491 \times 10^{-3}x^2 + 2.5346 \times 10^{-1}x + 4.2504 \\
\phi_4(x) &= 5.2187 \times 10^{-4}x^3 - 2.5865 \times 10^{-2}x^2 + 8.9327 \times 10^{-1}x + 3.6461 \\
\phi_5(x) &= -5.9217 \times 10^{-5}x^3 + 1.1761 \times 10^{-2}x^2 - 5.0808 \times 10^{-2}x + 3.1368 \\
\phi_6(x) &= 2.2683 \times 10^{-4}x^3 - 4.1523 \times 10^{-3}x^2 + 7.0504 \times 10^{-2}x + 3.4485 \qquad (4)
\end{aligned}$$

*III. Contact Detection*

With the relative angle between segments known, the orientation of each segment can be constructed by rotating the points defining the segment's vertices by the appropriate angle and translating them such that each segment is positioned with respect to the previous segment as shown in Fig. 11. Angles greater than the maximum angle allowed by the foot geometry are capped at the maximum value. The same process is then repeated for the opposing foot but with the rotation angles reversed. The transformation is given in Eqn. 5 where $P_{i,n}$ is the original vertex $n$ of segment $i$, $P'_{i,n}$ is the transformed vertex, and $\phi_{i_{total}}$ is the sum of the first $i$ segment angles. Figure 12 shows an example configuration.

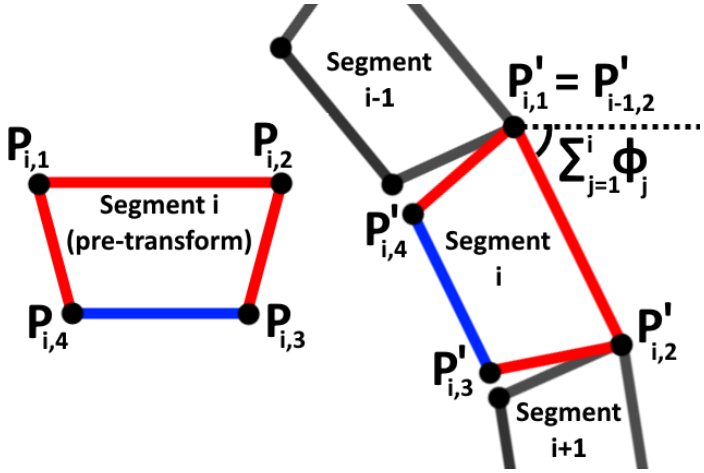


**Fig. 11 A foot is assembled by rotating and translating each segment into its current position and orientation.**

$$P'_{i,n} = \begin{bmatrix} \cos(\phi_{i_{total}}) & \sin(\phi_{i_{total}}) \\ -\sin(\phi_{i_{total}}) & \cos(\phi_{i_{total}}) \end{bmatrix} P_{i,n} + (P'_{i-1,2} - P_{i,1}) \quad (5)$$

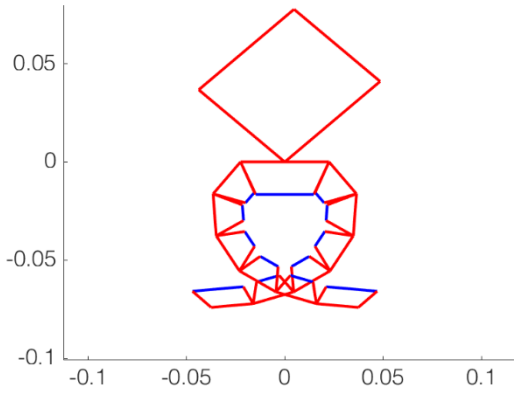


**Fig. 12 Example configuration of the four-bar linkage and two feet. Blue line segments are the segment surfaces used for contact detection.**

To detect contact between the foot segments and objects with polygonal cross-sections, each edge of the polygon is tested for contact with the inner surface of each segment. The direction vector of the force exerted by the segment on the polygon is in most cases normal to the edge. However, if the contact point is near a vertex of the polygon then the force direction is normal to the inner surface of the segment; see Fig. 13.

To detect contact between segments and circular cross-sections, the center of the circle is orthogonally projected onto each foot segment. If the projected point lies both on the segment and inside the circle, or if an endpoint of the segment is inside the circle, then contact has occurred. As shown in Fig. 13, the force direction vector points from the contact point toward the center of the circle. As the simulation evolves, contact detection is carried out at each step of tendon displacement. If a segment comes into contact with an object, that segment and all previous segments are fixed in place for the remainder of the simulation. If every segment has been fixed in place, the four-bar geometry is likewise fixed in place because the tendon is unable to displace any further. However, the cable tension can still continue to increase until constrained by the UAV weight.

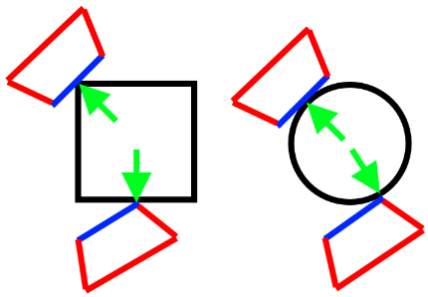

**Fig. 13 Directions of contact forces applied by object to a foot segment**

*IV. Force Calculations*

The net moment exerted by each segment on the object is zero when the segment makes initial contact because the moment acting on the segment is equal to the bending moment generated by the cable tendon. As tension increases after the segment has made contact, the tendon moment created by the tension increases while the bending moment remains constant (segment angle remains constant). By subtracting the tendon moment when contact was first made from the tendon moment at a later state, the magnitude of the unbalanced moment acting on the object can be determined from

$$M_T(x) = |\boldsymbol{r_T}| T(x) \cos\left(\tfrac{1}{2}\phi_{max} - \tfrac{1}{2}\phi(x)\right) \text{ and} \quad (6)$$

$$M_F(x) = M_T(x) - M_E(x) = M_T(x) - M_T(x_c) = |\boldsymbol{r_T}|\left(T(x) - T(x_c)\right) \cos\left(\tfrac{1}{2}\phi_{max} - \tfrac{1}{2}\phi(x)\right) \quad (7)$$

where $T(x)$ is the tendon tension, $M_T(x)$ is the moment applied by the tendon on the segment, $M_F(x)$ is the moment applied by the object on the segment, $M_E(x)$ is the external moment applied on the segment from contact with the previous segment, $x_c$ is the value of $x$ when the segment first made contact with the object, and $\boldsymbol{r_T}$ is the displacement vector from the segment's pivot point to the point where the tendon enters the segment; see Fig. 14.

If a subsequent segment has also made contact with the object, an additional moment exists and must be subtracted from $M_F$

$$M_{F_{net}} = M_F - \sum_{j=i+1}^{N} \left| \boldsymbol{r}_{F_{ij}} \times \boldsymbol{F}_j \right| \quad (8)$$

where $M_{F_{net}}$ is the moment created by the contact force, **F** (shown in Fig. 14), between the object and segment $i$ (only), $\boldsymbol{r}_{F_{ij}}$

is the displacement vector between the pivot point of segment $i$ and the contact point of the force of the object **o**n segment $j$, and $\boldsymbol{F_j}$ is the force on segment $j$.

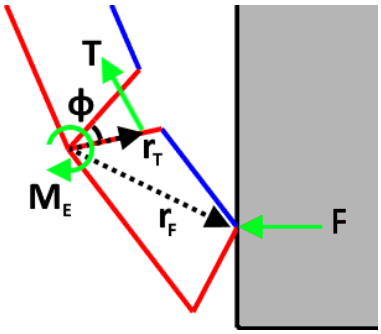


**Fig. 14 Diagram of the forces and moments acting on a foot segment that contribute to moment equilibrium with respect to the pivot point**

Given the moment exerted on the object and the direction vector of the applied force found during contact detection, the magnitude of the applied force can be computed using

$$F_i = \frac{M_{F_{net}}}{\left|\boldsymbol{r}_{\boldsymbol{F_{ii}}} \times \widehat{\boldsymbol{F}}_{\boldsymbol{i}}\right|} \qquad (9)$$

where $\widehat{\boldsymbol{F}}_{\boldsymbol{i}}$ is a unit vector in the direction of the force and $\boldsymbol{r}_{\boldsymbol{F_{ii}}}$ is the position vector between the pivot point of the segment and the contact point of the segment with the object.

The minimum weight of the UAV necessary to reach a given configuration state can be computed from the tendon tension or more useful, the maximum tendon tension for a given UAV weight. Assuming all links of the four-bar linkage have equal length, the tension to the weight relationship can be written as

$$W_{max} = -T_{max} \tan\left(\frac{\theta_1-\theta_4}{2}\right) \cos\left(\frac{\theta_1+\theta_4}{2}\right) \text{ or}$$

$$T_{max} = \frac{-W_{max}}{\tan\left(\frac{\theta_1-\theta_4}{2}\right)\cos\left(\frac{\theta_1+\theta_4}{2}\right)} \qquad (10)$$

where $W_{max}$ is the full weight of the UAV.

*V. Grasp Detection*

The feet are considered to be successfully grasping an object if the object is fully constrained from translational motion, *i.e.*, a component of a contact force from the feet to the object opposes motion. The angles of application of the contact forces are sorted and the differences between consecutive angles are then computed. A successful grip is indicated if no difference is greater than 180°. This grasp condition is given as

$$\psi = \text{sort}([\tan^{-1}(\tfrac{F_{y1}}{F_{x1}}), \tan^{-1}(\tfrac{F_{y2}}{F_{x2}}), \ldots \tan^{-1}(\tfrac{F_{yN}}{F_{xN}})]) \text{ and}$$

$$\max([\psi_2 \ldots \psi_N, \psi_1 + 360°] - [\psi_1, \psi_2 \ldots \psi_N]) < 180° \qquad (11)$$

where $F_{xi}$ and $F_{yi}$ are the components of each contact force vector and $\psi$ is the sorted list of force-application angles. If a grasp is successful, the minimum grasping force is defined by the smallest applied force that cannot be removed without breaking the grasp condition. A grasping force requirement can be implemented in which the minimum grasping force is compared to a specified threshold value.

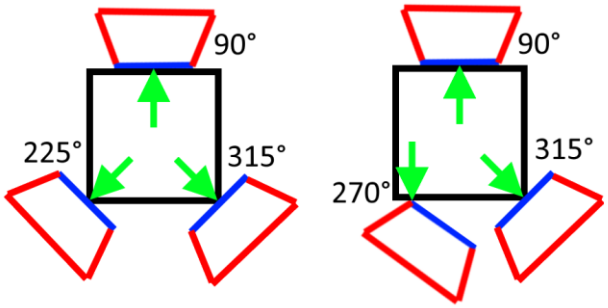


**Fig. 15 Two example grasp cases. The segments on the left have grasped the block successfully. Segments on the right have not because motion to the left is unopposed. Grasp is unsuccessful if the angle between any two consecutive contact forces (green) is greater than or equal to 180°.**

## SIMULATION RESULTS

The grasping behavior of a prototype perching landing gear mechanism was evaluated for landing target objects with a variety of cross-sectional shapes. Figure 16 shows simulation results (right) side-by-side with photos (left) of the prototype grasping corresponding real objects.

The model was then used to sweep over a range of objects of consistent shape but varying size, position, or angle and quantify the effectiveness of the landing gear at grasping each object in two ways: computing the minimum grasping force for a given UAV weight and computing the minimum UAV weight required to apply a successful grasp. Results corresponding to circular cross-sections of varying radius are shown in Figs. 17 and 18, respectively. Solid areas contain parameter pairs for successful grasp. The peaks arise when the numbers of segments involved in the grasp change and become engaged.

## CONCLUSION AND FUTURE WORK

This paper describes a hybrid empirical-numerical model of a bird-inspired landing gear system. Using empirical parameters identified for a specific prototype, simulations demonstrate the mechanical behavior of the mechanism in which the four-bar linkage collapses curling the feet. Results presented show the grasping of objects or various sizes and shapes. Force and moments generated are calculated and used to evaluate the success of the grasp. The model is validated by comparison to experiments.

This model can be used by UAV designers to identify objects and structures on which an air vehicle can land, perch, and take-off. They would be able to quantitatively relate the weight of the UAV to perching success.

We are continuing to extend this work by further exploring the design space and optimizing parameter selection to meet desired performance specifications for a range of perching targets.

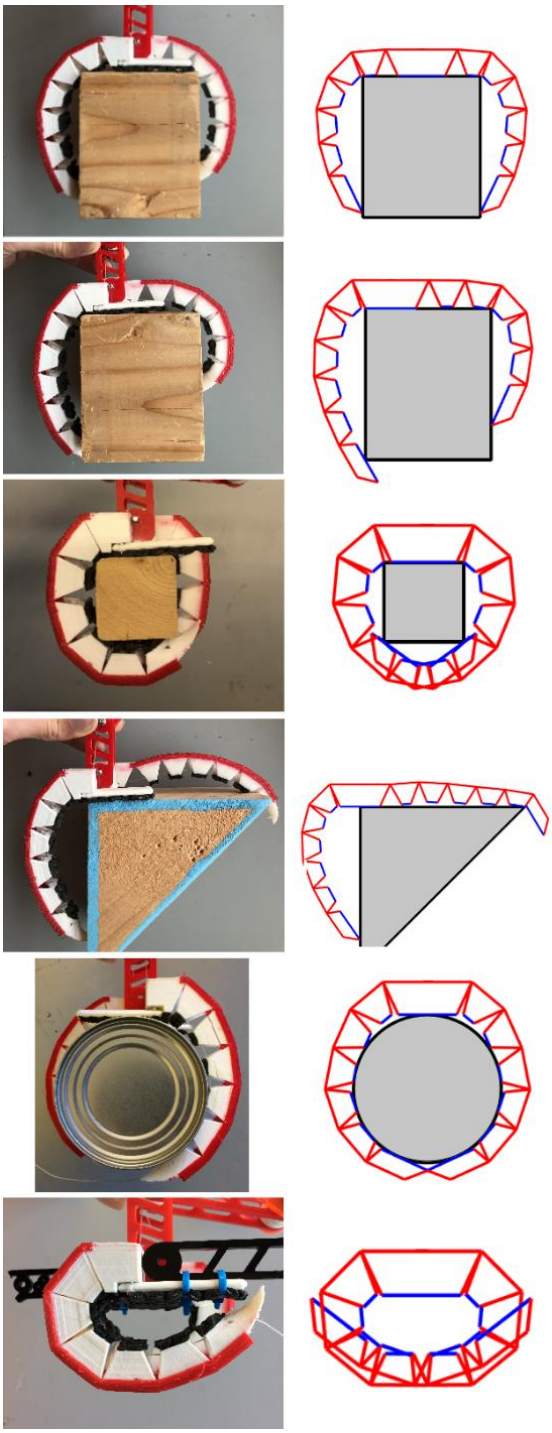

**Fig. 16 Validation of the simulated and real grasping behavior for a rectangular block, large, off-center rectangular block, small square block, triangular block, cylinder, and empty grasp.**

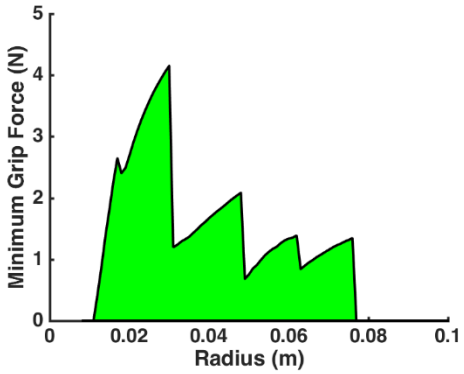


**Fig. 17 Minimum grip force for cylindrical objects of varying radius for a UAV weight of 11.6 N. Successful grasp parameter combinations occur in the solid (green) region. Zero grip force indicates unsuccessful grasp. The peaks are caused by transition between different numbers of segments involved in the grasp.**

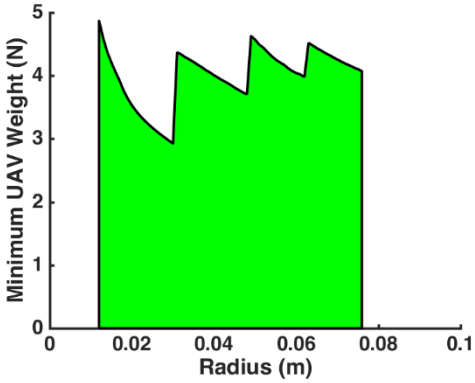


**Fig 18 Minimum UAV weight required to successfully grasp cylindrical objects of varying radius assuming minimum grip force threshold is 0 N. The solid (green) region indicates successful grasp.**

## REFERENCES


[1] Kovac, M., "Learning from Nature How to Land Aerial Robots." *Science* Vol. 352 No. 6288 (2016): pp. 895-896. DOI 10.1126/science.aaf6605.

[2] Robertson, D. K., and Reich, G. W., 2013, "Design and Perching Experiments of Bird-Like Remote Controlled Planes." *Proceeding of the 54th AIAA/ASCE/AHS/ASC Structures, Structural Dynamics, and Materials Conference*. AIAA 2013-1788. Boston, MA, April 8-11, 2013. DOI 10.2514/6.2013-1788.

[3] Nagrendran, A., Crowther, W., and Richardson, R. C., "Biologically Inspired Legs for UAV Perched Landing." *IEEE Aerospace and Electronic Systems Magazine*, Vol. 7 No. 2 (2012), pp. 4-13. DOI 10.1109/MAES.2012.6163608.

[4] Paranjape, A. A., Kim, J., Gandhi, N., and Chung, S.-J., 2011, "Experimental Demonstration of Perching by an Articulated Wing MAV." *Proceedings of the AIAA Guidance, Navigation, and Control Conference*. AIAA 2011-6403. Portland, OR, August 8-11, 2011. DOI 10.2514/6.2011-6403.

[5] Cory, R. and Tendrake, R., "Experiments in Fixed-Wing UAV Perching." *Proceedings of the AIAA Guidance, Navigation, and Control Conference and Exhibit*. Honolulu, HI, August 18-21 2008. DOI 10.2514/6.2008-7256.

[6] Culler, E. S., Thomas, G. C., and Lee, C. L., 2012, "A Perching Landing Gear for a Quadcopter," *Proceeding of the 53th AIAA/ASCE/AHS/ASC Structures, Structural Dynamics, and Materials Conference*. AIAA 2012-1722. Honolulu, HI, April 23-26 2012. DOI 10.2514/6.2012-1722.

[7] Ali Erbil, M., Prior, S. D., and Keane, A. J., "Design Optimisation of a Reconfigurable Perching Element for Vertical Take-Off and Landing Unmanned Aerial Vehicles." *International Journal of Micro Air Vehicles* Vol. 5 No. 3 (2013), pp. 207-228.

[8] Chi, W., Low, K. H., Hoon, K. H., and Tang, J., "An Optimized Perching Mechanism for Autonomous Perching with a Quadrotor." *Proceedings of the IEEE International Conference on Robotics and Automation*. Hong Kong, China, May 31-June 7, 2014. DOI 10.1109/ICRA.2014.6907306.

[9] Jiang, H., Pope, M. T., Hawkes, E. W., Christensen, D. L., Estrada, M. A., Parlier, A., Tran, R., and Cutkosky, M. R., "Modeling the Dynamics of Perching with Opposed-Grip Mechanisms." *Proceedings of the International Conference on Robotics and Automation.* Hong Kong, China, May 31-June 7, 2014. DOI: 10.1109/ICRA.2014.6907305.

[10] Burroughs, M. L., Beauwen Freckleton, K., Abbott, J. J., and Minor, M. A., "A Sarrus-Based Passive Mechanism for Rotorcraft Perching." *ASME Journal of Mechanisms and Robotics* Vol. 8 No. 1 (2015): pp. 011010. DOI 10.1115/1.4030672.

[11] Quinn, T. H., and Baumel, J. J., "The Digital Tendon Locking Mechanism of the Avian Foot (Aves)." *Zoomorphology* Vol 109 (1990): pp. 281-293. DOI 10.1007/BF00312195.

[12] Backus, S. B., Odhner, L. U., and Dollar, A. M., 2014, "Design of Hands for Aerial Manipulation Actuator Number and Routing for Grasping and Perching." *Proceeding of the IEEE/RSJ International Conference on Intelligent Robots and Systems*, Chicago, IL, September 14-18, 2014. DOI 10.1109/IROS.2014.6942537

[13] Backus, S. B., Sustaita, D., Odhner, L. U., and Dollar, A. M., "Mechanical Analysis of Avian Feet: Multiarticular Muscles in Grasping and Perching." *Royal Society Open Science*, Vol. 2 (2015), pp. 140350. DOI 10.1098/rosos.140350. 2015.

[14] Doyle, C. E., "Avian-Inspired Passive Landing Mechanisms for Perching Rotorcraft," MS Thesis. The University of Utah, Salt Lake City, UT. 2011.

[15] Doyle, C. E., Bird, J. J., Isom, T. A., Kallman, J. C., Bareiss, D. F., Dunlap, D., J., King, R. J., Abbott, J. J., and Minor, M. A., "An Avian-Inspired Passive Mechanism for Quadrotor Perching." *IEEE/ASME Transactions on Mechatronics*. Vol. 18 No. 2 (2013): pp. 506-517. DOI 10.1109/TMECH.2012.2211081.

[16] Xie, P., and Ma, O., "Grasping Analysis of a Bio-Inspired UAV/MAV Perching Mechanism." Proceeding of the *ASME 2013 International Mechanical Engineering Congress and Exposition*. IMECE2013-66526: pp. V001T01A012. San Diego, CA, November 15-21, 2013. DOI 10.1115/IMECE2013-66526.

[17] Xie, P., Ma, O., Zhang, L., and Zhao, Z., "A Bio-Inspired UAV Leg-Foot Mechanism for Landing, Grasping, and Perching Tasks." *Proceeding of the AIAA Atmospheric Flight Mechanics Conference, AIAA SciTech Forum*. AIAA 2015-1689. Kissimmee, FL, January 5-9, 2015. DOI 10.2514/6.2015-1689.

[18] Tieu, M., Michael, D.M., Pflueger, J.B., Sethi, M.S., Shimazu, K.N., Anthony, T.M., and Lee, C.L., "Demonstrations of Bio-Inspired Perching Landing Gear for UAV's." *Proceeding of the SPIE Smart Structures and Materials + Nondestructive Evaluation and Health Monitoring, Bioinspiration, Biomimetics, and Bioreplication VI*. 97970X. Las Vegas, NV, March 20-24, 2016. DOI 10.1117/12.2218167.

[19] Gardner, J. F. *Simulations of Machines Using MATLAB and SIMULINK*. Wadsworth Group Pacific Grove, CA (2001).

## ACKNOWLEDGMENTS

The authors gratefully acknowledge financial support from the MA Space Grant Consortium and the Olin College Intellectual Vitality Program. Mindy Tieu, Duncan Michael, Jeff Pflueger, Manik Sethi, Kelli Shimazu, and Tatiana Anthony designed, fabricated, and tested the landing-gear system prototype.

 